

Characterization of compressible fluctuations in solar wind streams dominated by balanced and imbalanced turbulence: Parker Solar Probe, Solar Orbiter and Wind observations

C.A. GONZÁLEZ ,¹ C. GONZALEZ ,¹ AND A. TENERANI ,¹

¹*Department of Physics, The University of Texas at Austin, Austin, TX 78712, USA*

ABSTRACT

Characterizing compressible fluctuations in the solar wind is essential for understanding their role in solar wind acceleration and heating, yet their origin and evolution across different turbulence regimes remain poorly understood. In this study, we carry out a statistical analysis of the properties of compressible fluctuations in solar wind dominated by balanced and imbalanced turbulence. Using in-situ measurements from Wind, Solar Orbiter and Parker Solar Probe, we investigate the scale dependence of density and magnetic field fluctuations and their correlations with plasma beta and radial distance. Our results indicate that solar wind compressibility is likely affected by both expansion effects and compressible dynamics governed by local plasma conditions. The non-Alfvénic wind is dominated by anti-correlated fluctuations, whereas the Alfvénic wind contains a mixture of correlated and anti-correlated fluctuations, though the latter remain prevalent. While the anti-correlated component is consistent with MHD slow magnetosonic modes, the correlated (fast mode-like) component is not reproduced by predictions from either linear MHD theory or nonlinear models of forced compressible fluctuations. Nevertheless, the dominant slow mode component explains the observed dependence of $\delta B_{\parallel}/\delta B_{\perp}$ on β and the enhanced density fluctuations measured by Parker Solar Probe. This further suggests that slow mode waves contribute significantly to the compressible energy budget near the Sun and may play an important role in solar wind heating and acceleration close to the sun.

1. INTRODUCTION

The solar wind, the continuous plasma outflow from the Sun's corona into interplanetary space, is largely permeated by low-frequency Alfvénic turbulence characterized by strong correlations between plasma velocity and magnetic field variations across a broad range of temporal and spatial scales (J. Belcher & L. Davis Jr 1971; C.-Y. Tu & E. Marsch 1995; R. Bruno & V. Carbone 2013). These Alfvénic fluctuations, found in wind streams originating from coronal holes, are primarily propagating away from the Sun and they contain enough energy to heat the plasma, although the turbulent dissipation and heating mechanisms are not yet fully understood. A smaller population of sunward-propagating fluctuations is also present, and the imbalance between outward and inward wave populations tends to decrease with radial distance (W. H. Matthaeus & M. L. Goldstein 1982; B. Bavassano et al. 2000). The relative proportion of counter-propagating fluctuations determines the strength of nonlinear interactions and, therefore, the

overall turbulent state (B. D. Chandran 2008; A. A. Schekochihin 2022a).

The Alfvénic solar wind, characterized by imbalanced turbulence, also contains a smaller fraction of compressible fluctuations at inertial and kinetic scales (B. Bavassano & R. Bruno 1989; C.-Y. Tu & E. Marsch 1994). These fluctuations generally involve variations in magnetic and thermal pressure. The latter, acting through density fluctuations, generates Alfvén velocity gradients that can enhance wave reflection and dissipation in plasmas. Indeed, incompressible reflection-driven turbulence alone may be insufficient to heat the corona and accelerate the solar wind (S. R. Cranmer & M. E. Molnar 2023; A. Verdini et al. 2019). Compressible effects, on the other hand, could provide the additional reflection required to enhance the turbulent cascade and the associated heating rate (M. Asgari-Targhi et al. 2021; A. Verdini et al. 2019). They can also trigger other dynamical processes such as Alfvén wave instabilities (N. F. Derby Jr 1978) or nonlinear wave steepening (R. H. Cohen & R. M. Kulsrud 1974), that contribute further to heating (A. González et al. 2021; C. González et al. 2023, 2024).

Corresponding author: C.A. González
 carlos.gonzalez1@austin.utexas.edu

The compressible component of the solar wind has been characterized in past work by analyzing the correlation between changes in thermal and magnetic pressures, typically represented as fluctuations in plasma density and the magnetic field magnitude. The mode polarization is identified by its correlation, being positive for fast modes and negative for slow magnetosonic modes, respectively. Observations at 1 au and at larger heliocentric distances have shown that compressible fluctuations typically display negative correlation (U. Villante & M. Vellante 1982; D. Roberts et al. 1987; B. Bavassano et al. 2004), which has been interpreted as a signature of non-propagating pressure-balanced structures (PBS) or MHD/kinetic slow modes (ion-acoustic and mirror modes) (S. Yao et al. 2011; G. Howes et al. 2012; K. Klein et al. 2012; Y. Narita & E. Marsch 2015; D. Verscharen et al. 2017).

On the other hand, Helios measurements between 0.3 and 1 au revealed a mixture of fast and slow-mode waves (C.-Y. Tu & E. Marsch 1994). Observations during the first PSP encounters detected the presence both modes, with a greater contribution from the slow mode (C. Chaston et al. 2020). In contrast, S. Zhao et al. (2021) showed that most of the power is associated with the fast mode, while a smaller fraction is attributed to slow modes. Additionally, C. Chen et al. (2020) reported a reduction in the slow-mode component in the inner heliosphere. On the other hand, recent measurements in the inner heliosphere have revealed enhanced levels of density fluctuations which have been associated with slow modes (L.-L. Zhao et al. 2025). Remote sensing observations of the outer corona also indicate increased relative density fluctuations (M. Hahn et al. 2018; M. Miyamoto et al. 2014). Thus, to date, no conclusive observations have been established on which wave mode dominates closer to the Sun. Furthermore, 3D simulations of these regions demonstrate both the development of density fluctuations and the coexistence of fast and slow waves (S. Chiba et al. 2025).

Among the various mechanisms that can generate compressible fluctuations in plasmas, those associated with Alfvénic fluctuations are particularly relevant in the context of Alfvénic solar wind. As Alfvén waves reach large amplitude, nonlinearities become stronger, enabling different parametric instabilities (R. Z. Sagdeev & A. A. Galeev 1969; N. F. Derby Jr 1978; M. L. Goldstein 1978; J. V. Hollweg 1994; B. Buti et al. 2000; L. Matteini et al. 2010). Moreover, density fluctuations can also be driven by envelope-modulated Alfvén waves that arise from the plasma's response to variations in wave magnetic pressure (R. H. Cohen & R. M. Kulsrud 1974). These mechanisms produce fast and/or slow

modes depending on different plasma parameters such as the plasma beta and the propagating angle (J. V. Hollweg 1971; R. H. Cohen & R. M. Kulsrud 1974; S. R. Spangler & J. P. Sheerin 1982; T. Hada 1993; A. Mallet et al. 2021). In addition, plasma instabilities, such as beam and/or flow instabilities, can also generate compressible fluctuations that could be relevant in the solar wind scenario (S. P. Gary 1993), although these are typically at kinetic scales.

In this work, we present a statistical analysis of compressible fluctuations at inertial range scales in the solar wind using data from Parker Solar Probe, Solar Orbiter and Wind missions, covering radial distances from 10 solar radii out to 1 au. Our goal is to investigate the evolution and nature of compressibility and its dependence on fluctuations amplitude. Although our primary goal is to characterize compressibility in the Alfvénic, imbalanced wind, we examine streams dominated by both balanced and imbalanced turbulence for comparison.

This paper is organized as follows: in Section 2, we describe interval selection procedure, the dataset used in this work and our methodology to study compressible fluctuations; Section 3 outlines the main results, focusing on the scale dependence of magnetic and density fluctuations, and their relationship with fluctuation amplitude for both balanced and imbalanced turbulent solar wind. We also analyzed their dependence on plasma beta and examine the correlation between thermal and magnetic pressure fluctuations; finally, Section 4 summarizes our conclusions and discusses the broader implications of our findings.

2. DATA AND METHODOLOGY

We investigated the properties of compressible fluctuations in the solar wind by using *in-situ* measurements from three missions located in different regions of the heliosphere. At 1 au, we used data from the Wind spacecraft from 1999 to 2018, including 3-second resolution ion measurements from the plasma instrument (3DP) (R. Lin et al. 1995) and magnetic field data from the MFI instrument (R. Lepping et al. 1995). In the inner heliosphere, we used Parker Solar Probe (PSP) observations from 2019 to 2024 (Encounter 4th to 21st). We used magnetic field measurements from the FIELDS instrument suite (S. Bale et al. 2016) and ion moments from the SPAN-I analyzer (R. Livi et al. 2022), along with electron density estimates from the quasi-thermal noise (QTN) signal measured by the Radio Frequency Spectrometer (M. Moncuquet et al. 2020). We used data within heliocentric distances less than 0.25 au to avoid low-quality ion moment data associated with field-of-view in SPAN-I instrument. All data is sampled at

3-second resolution. Additionally, we included Solar Orbiter (SolO) data collected between 2022 and 2024, covering radial distances from 0.3 to 1 au. For SolO, we used 4-second resolution magnetic field measurements from the MAG instrument (T. Horbury et al. 2020) and proton moments derived from the Solar Wind Analyzer–Proton and Alpha Sensor (SWA-PAS) (C. Owen et al. 2020).

In this study, we classified solar wind streams based on the normalized cross-helicity

$$\sigma_c = (\langle |\mathbf{z}^+|^2 \rangle - \langle |\mathbf{z}^-|^2 \rangle) / (\langle |\mathbf{z}^+|^2 \rangle + \langle |\mathbf{z}^-|^2 \rangle),$$

which measures the relative contribution of outward and inward Alfvén waves. The brackets $\langle \dots \rangle$ denote the moving average over a given time window and $\mathbf{z}^\pm = \delta \mathbf{u} \pm \delta \mathbf{B} / \sqrt{(\mu_0 \rho)}$ are the Elsässer variables. Here, ρ is calculated from QTN data for PSP and σ_c is calculated over a 2-hour window. Intervals where $|\sigma_c| < 0.25$ (balanced turbulence) are classified as non-Alfvénic while those with $|\sigma_c| > 0.75$ (imbalanced turbulence) are classified as Alfvénic wind. We do not distinguish between fast- and slow-Alfvénic wind since both display similar turbulence properties (R. D’amicis et al. 2019; D. Perrone et al. 2020; R. D’Amicis et al. 2020).

To examine the properties of large-scale, inertial range fluctuations, we started with 5 days long intervals and selected sub-intervals in which the normalized cross-helicity, σ_c , remains nearly constant over intervals much longer than the characteristic timescale of the fluctuations. Specifically, we required that σ_c be approximately constant over a time interval of at least $30\tau_c$, where τ_c denotes the correlation time (the outer scale of the turbulent fluctuations). The correlation time is determined from the autocorrelation function of the magnetic field fluctuations,

$$f(\tau) = \langle \delta \mathbf{B}(t + \tau) \cdot \delta \mathbf{B}(t) \rangle_{\text{interval}},$$

where $\delta \mathbf{B}(t) = \mathbf{B}(t) - \langle \mathbf{B} \rangle_{\text{interval}}$, and it is defined as the time lag at which $f(\tau)$ decays to $1/e$ of its initial value. Using this methodology, we identified more than 801 streams, distributed as follows: for Wind, 249 Alfvénic and 56 non-Alfvénic intervals; for SolO, 219 Alfvénic and 67 non-Alfvénic intervals; and for PSP, 181 Alfvénic and 29 non-Alfvénic intervals. When explicitly stated, we also employed a second dataset composed of a larger number of sub-intervals, obtained by dividing the long intervals into shorter segments of 2–3 hours. This procedure enables us to investigate inertial-range properties while enhancing statistical robustness. Furthermore, we removed sub-intervals associated with Coronal Mass Ejections (CMEs) listed in the published catalog

by C. Möstl et al. (2020), as well as intervals characterized by low density in which the QTN electron density falls below the instrumental limit of 100 cm^{-3} (M. Moncuquet et al. 2020). For the Alfvénic cases, this yields 4117 short sub-intervals for Wind, 2471 for SolO, and 784 for PSP. For the non-Alfvénic cases, we obtain 677 short sub-intervals for Wind, 154 for SolO, and 30 for PSP, corresponding to a total duration of 17201 hours.

We characterized the amplitude of fluctuations and compressibility using the following quantities: the normalized root-mean-square (rms) amplitude of magnetic fluctuations, $\delta B / \langle |\mathbf{B}| \rangle = [\sum \langle (B_i - \langle B_i \rangle)^2 \rangle / \sum \langle B_i \rangle^2]^{1/2}$, the normalized rms of the magnetic field magnitude fluctuations (a proxy for magnetic compressibility) $\langle \delta |\mathbf{B}|^2 \rangle^{1/2} / \langle |\mathbf{B}| \rangle = \langle (|\mathbf{B}| - \langle |\mathbf{B}| \rangle)^2 \rangle^{1/2} / \langle |\mathbf{B}| \rangle$, and the normalized rms values of density fluctuations $\langle \delta n^2 \rangle^{1/2} / \langle n \rangle = \langle (n - \langle n \rangle)^2 \rangle^{1/2} / \langle n \rangle$. We also quantified the relationship between compressible fluctuations and the proton plasma beta ($\beta = 2\mu_0 n k_B T_p / |\mathbf{B}|^2$, with k_B the Boltzmann constant, T_p the proton temperature, and μ_0 the vacuum permeability).

In addition, we computed the angle between wind velocity and mean magnetic field

$$\theta_{kB_0} = \cos^{-1} \left(\frac{\mathbf{V}_{SW} \cdot \langle \mathbf{B} \rangle}{\langle |\mathbf{B}| \rangle \|\mathbf{V}_{SW}\|} \right),$$

which, under the Taylor hypothesis, provides additional information about the direction in which the fluctuations are sampled relative to the mean magnetic-field direction. The statistics on the propagation angle (not shown) indicate that Alfvénic intervals are typically observed in field-aligned wind, with the most probable values of θ_{kB_0} around 30° and 150° for both the Wind and SolO datasets. In contrast, non-Alfvénic wind is found at very oblique angles, approximately $\theta_{kB_0} \sim 90^\circ$. Instead, PSP has almost consistently detected field-aligned wind for both types of winds.

To identify fluctuations of the fast and slow mode type, we used the shorter sub-interval dataset to quantify the correlation between normalized magnetic pressure fluctuations ($\delta |\mathbf{B}|^2 / \langle |\mathbf{B}|^2 \rangle = \langle (|\mathbf{B}|^2 - \langle |\mathbf{B}|^2 \rangle) \rangle / \langle |\mathbf{B}|^2 \rangle$) and density fluctuations $\delta n / \langle n \rangle$. Although such correlations should be calculated with fluctuations of thermal pressure, the second order moment measurements are often contaminated with outliers. To mitigate this issue, we assumed isothermal conditions and considered fluctuations in density instead.

We used wavelet analysis (C. Torrence & G. P. Compo 1998) to compute the coherence between $\delta |\mathbf{B}|^2 / \langle |\mathbf{B}|^2 \rangle$

Mission	Alfvénic								
	$\langle \mathbf{B} \rangle$	$ \langle \mathbf{B} \rangle $	$\langle \delta \mathbf{B}_\perp ^2 \rangle^{1/2}$	$\langle \delta \mathbf{B}_\parallel ^2 \rangle^{1/2}$	$\langle \delta \mathbf{B} ^2 \rangle^{1/2}$	$\frac{\langle (\delta \mathbf{B} ^2)^2 \rangle^{1/2}}{\langle \mathbf{B} ^2 \rangle}$	$\langle n \rangle$	$\langle (\delta n)^2 \rangle^{1/2}$	$\frac{\langle (\delta n)^2 \rangle^{1/2}}{\langle n \rangle}$
PSP	-2.03 ± 0.04	-2.08 ± 0.04	-1.74 ± 0.07	-1.41 ± 0.12	-1.72 ± 0.07	0.80 ± 0.11	-1.89 ± 0.14	-1.95 ± 0.10	-0.10 ± 0.12
SolO	-1.56 ± 0.01	-1.56 ± 0.01	-1.61 ± 0.01	-1.61 ± 0.02	-1.61 ± 0.01	0.22 ± 0.02	-2.12 ± 0.01	-2.29 ± 0.02	-0.17 ± 0.01
Combined	-1.66 ± 0.01	-1.69 ± 0.01	-1.55 ± 0.01	-1.41 ± 0.01	-1.54 ± 0.01	0.40 ± 0.01	-2.14 ± 0.01	-2.55 ± 0.01	-0.43 ± 0.01
Non-Alfvénic									
PSP	-1.77 ± 0.34	-1.72 ± 0.48	-1.47 ± 0.49	-1.63 ± 0.64	-1.51 ± 0.50	-0.15 ± 0.63	-3.75 ± 0.85	-2.92 ± 0.68	1.03 ± 0.71
SolO	-1.63 ± 0.05	-1.53 ± 0.06	-1.82 ± 0.07	-1.98 ± 0.08	-1.87 ± 0.07	-0.29 ± 0.07	-2.21 ± 0.06	-2.53 ± 0.08	-0.34 ± 0.06
Combined	-1.43 ± 0.05	-1.38 ± 0.05	-1.69 ± 0.06	-1.34 ± 0.07	-1.55 ± 0.06	0.24 ± 0.06	-1.73 ± 0.07	-1.99 ± 0.08	-0.29 ± 0.06

Table 1. Radial dependence of the mean and rms of different quantities. Power law scalings are given separately for each mission and for the combined dataset, for both Alfvénic and non-Alfvénic solar intervals.

and $\delta n/\langle n \rangle$,

$$C(t, \omega)_{\delta|\mathbf{B}|^2, \delta n} = S[W_{\delta|\mathbf{B}|^2}^*(t, \omega) W_{\delta n}(t, \omega)],$$

and the phase

$$\phi(t, \omega) = \tan^{-1} \left(\frac{\text{Im}[C(t, \omega)_{\delta|\mathbf{B}|^2, \delta n}]}{\text{Re}[C(t, \omega)_{\delta|\mathbf{B}|^2, \delta n}]} \right).$$

Here, $W(t, \omega)$ corresponds to the Morlet continuous wavelet transform, and t and ω denote time and the frequency, with the relation $\omega \propto 1/a$ where a is the wavelet scale. The operator S is a smoothing function applied in both the time and frequency domains. From time-frequency coherence and phase spectrograms, we compute the mean values of $C(t, \omega)$ and $\phi(t, \omega)$ within the frequency band of interest $1/5 \leq \omega \tau_c \leq 1$, where τ_c is the correlation time of the interval.

3. RESULTS

I. Radial scalings and scale dependence

As expected from the overall expansion, both the mean magnetic field and the proton density decrease with radial distance. Table 1 reports the best fit parameters for several quantities, assuming a power-law dependence on the radial distance, R^α . We list the resulting power-law index α for each individual dataset and for the combined set of observations. For the fitting procedure, we restricted the analysis to the short sub-intervals of the PSP and SolO datasets and calculated fluctuations and averages over a time scale $\tau = 5\tau_c$ (corresponding to roughly $\tau \sim 0.68 \pm 0.44$ hours depending on radial distance).

According to WKB theory, $\langle |\delta \mathbf{B}|^2 \rangle^{1/2} \propto R^{-1.5}$, while the radial mean magnetic field $|\langle \mathbf{B} \rangle| \sim R^{-2}$. The scaling of $|\langle \mathbf{B} \rangle|$ is consistent with a predominantly radial mean magnetic field during Alfvénic intervals in PSP, but including SolO measurements at larger distances yields a radial dependence of $R^{-1.66}$. On the other hand, the non-Alfvénic wind shows a slower decay of $R^{-1.43}$. These deviations from a purely radially expanding flux

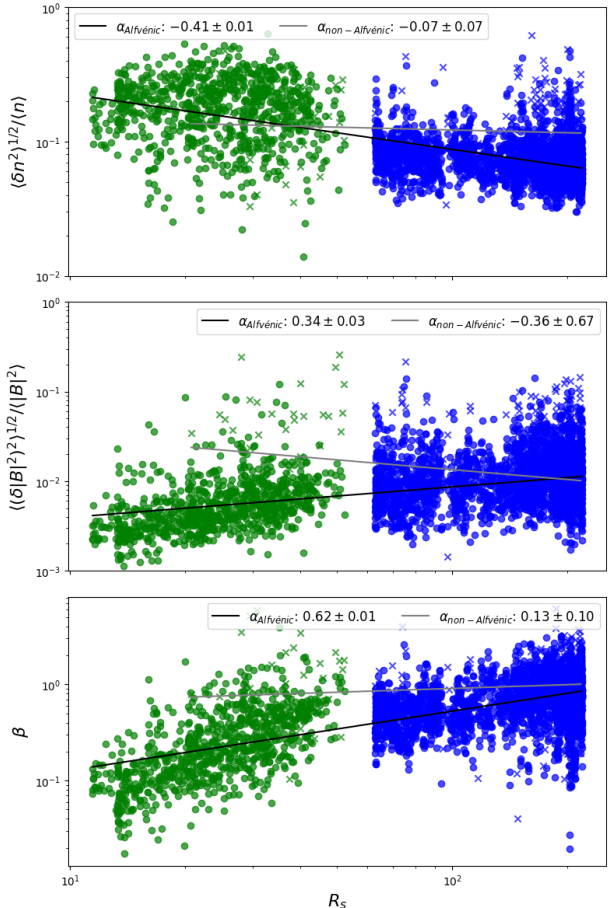


Figure 1. Values of normalized rms of the density (top panel) and magnetic pressure fluctuations (middle panel) and proton beta (bottom panel) averaged over each short sub-interval as a function of radial distance. Green and blue color correspond to PSP and SolO datasets, respectively. Alfvénic sub-intervals are marked with circles and non-Alfvénic intervals with crosses. The power law coefficients from the best-fit curves are reported in the legend. The corresponding linear regression lines are plotted in black for the Alfvénic intervals and in gray for the non-Alfvénic intervals.

tube are likely associated with the Parker spiral geometry and possibly other large-scale structures.

For the rms magnetic fluctuation amplitude, we obtain $\langle |\delta\mathbf{B}|^2 \rangle^{1/2} \propto R^{-1.54}$ and $\langle |\delta\mathbf{B}|^2 \rangle^{1/2} \propto R^{-1.55}$ for Alfvénic and non-Alfvénic wind, respectively, in good agreement with earlier (B. Bavassano et al. 1982; A. Tenerani et al. 2021) and close to the WKB prediction (the faster decay is typically observed as the frequency of fluctuations increases). However, when fluctuations are decomposed into perpendicular and parallel components, we find $\langle |\delta\mathbf{B}_\perp|^2 \rangle^{1/2} \propto R^{-1.55}$ and $R^{-1.69}$, and $\langle |\delta\mathbf{B}_\parallel|^2 \rangle^{1/2} \propto R^{-1.41}$ and $R^{-1.34}$ for Alfvénic and non-Alfvénic wind, respectively. In the Alfvénic wind (top three rows in Table 1), which is generally expected to follow WKB trends at large scales, the perpendicular component decays approximately as predicted (third column in Table 1), whereas the parallel fluctuating component displays a slower decay rate observed in both the PSP and the combined data (fourth column in Table 1). This slower radial decay of field-aligned fluctuations with respect to the perpendicular ones is expected for incompressible, spherically polarized Alfvénic fluctuations with an exactly constant B^2 , as a result of their coupling to the guiding magnetic field (L. Matteini et al. 2024) — although the specific decay rate of $\langle |\delta\mathbf{B}|^2 \rangle^{1/2}$ in general depends on the geometry of the mean field and can be affected by Parker's spiral effects. Nevertheless, the observed deviations from WKB of the field-aligned fluctuations could also indicate the generation of additional (subdominant) compressible fluctuations during the expansion. The latter interpretation is consistent with the observed increase in relative magnetic-pressure fluctuations, which grow more rapidly in PSP and in the combined data set than in SolO (sixth column in Table 1), reflecting the same trend of $\langle |\delta\mathbf{B}_\parallel|^2 \rangle^{1/2}$. In contrast, the radial evolution of the density in the Alfvénic wind is close to that expected from mass-flux conservation, with a scaling $\propto R^{-2.14}$, while the non-Alfvénic wind shows a shallower decrease of $R^{-1.73}$. The overall fitting of different plasma quantities are consistent with previous studies (B. A. Maruca et al. 2023).

Despite the radial regression trends discussed above, fluctuations related to compressibility display substantial variability from one stream to another and are significantly scattered as a function of radial distance. Figure 1 presents the normalized rms of the proton density and magnetic pressure fluctuations as a function of radial distance, while the bottom panel shows the mean plasma beta for each sub-interval. Although fitting the combined data indicates some dependence on radial distance, data points are highly dispersed around the regression line and only weakly correlated with R , with Pearson correlation coefficient $\text{corr} < 0.5$ in all cases.

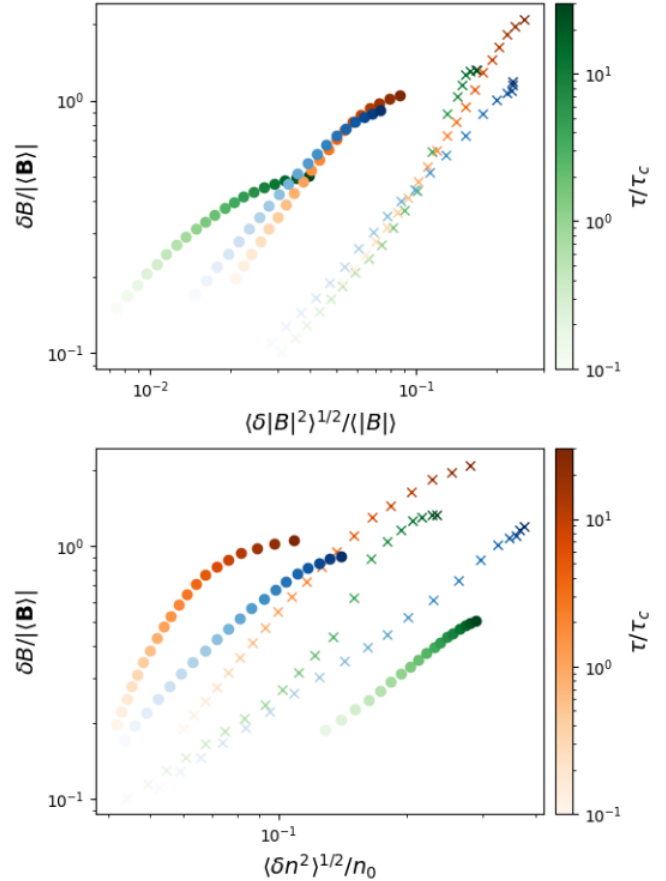


Figure 2. Scatter plots showing the ensemble-averaged distribution of the normalized rms of magnetic field fluctuations amplitude vs the ensemble-averaged normalized rms of density (top panel) and magnetic field magnitude (bottom panel) fluctuations obtained from the long-interval datasets. Circles and crosses denote Alfvénic and non-Alfvénic solar wind streams, respectively. The time scale τ is color coded and distinct colormaps are used to indicate PSP (green), SolO (blue) and Wind (orange) datasets.

We analyzed the scale-dependent properties of fluctuations indicative of compressibility within the inertial range, corresponding to scales $0.1 < \tau/\tau_c < 30$, using the long-interval dataset. The ensemble of time series of the magnetic field, magnetic field magnitude, and density fluctuation amplitudes were used to construct the probability density functions (PDFs) shown in Fig. A1. The mean values of these PDFs are reported in Fig. 2, where different color shades represent increasing scale τ from light to dark color. Figure 2 displays scatterplots of the rms of magnetic field fluctuations versus the rms of the normalized magnetic field-magnitude fluctuations (top panel) and versus the rms density fluctuations (bottom panel). Circles represent Alfvénic intervals, while crosses represent non-Alfvénic wind.

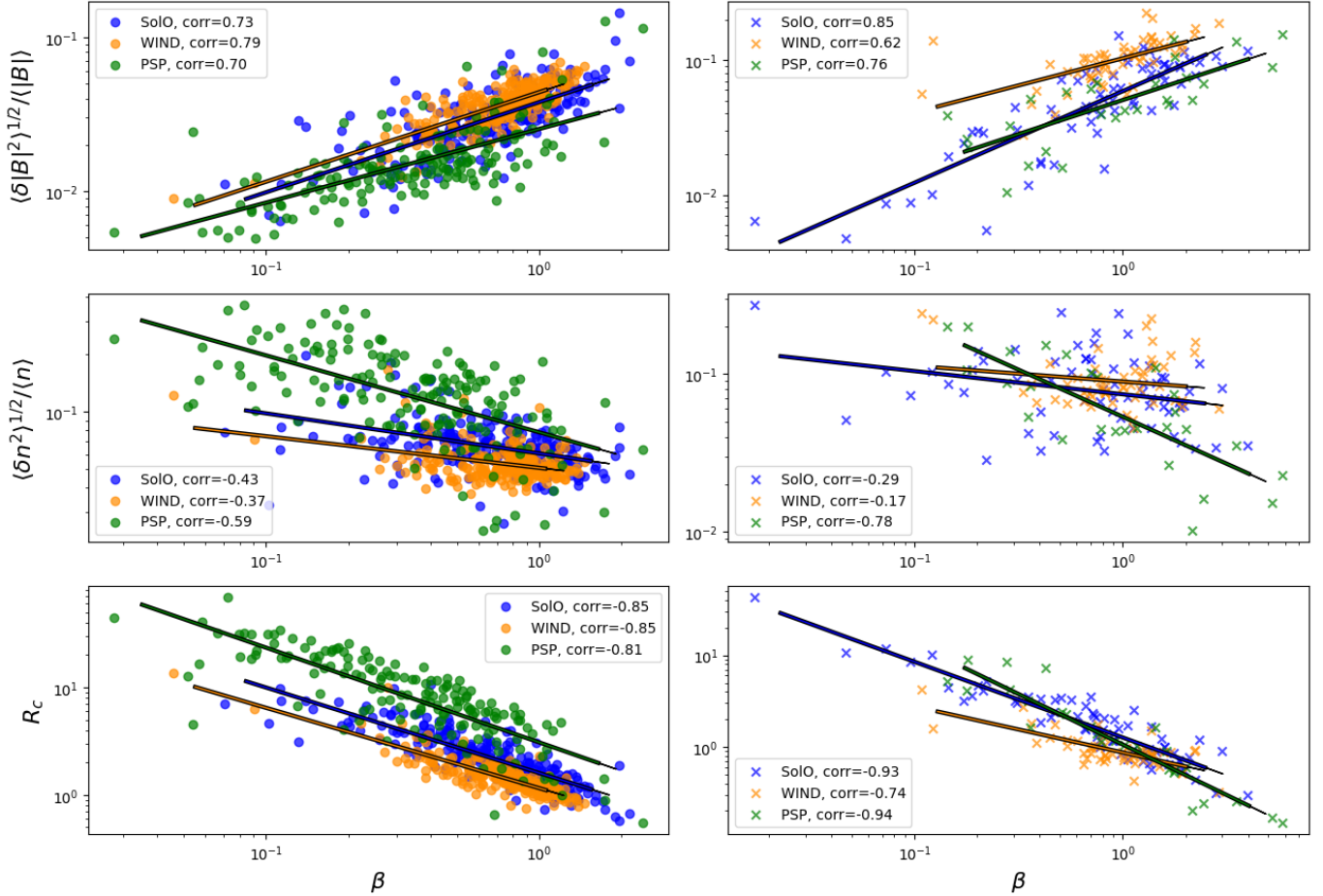


Figure 3. Correlation between compressible fluctuations and plasma beta. The left column shows results for Alfvénic intervals, while the right column corresponds to non-Alfvénic intervals. Magnetic field magnitude fluctuations are shown in the top panels, density fluctuations in the middle panels, and their ratio in the bottom panels. The Pearson correlation for each dataset is reported in the legends. Thick lines represent the linear regression fit for each mission, reported here as a reference for general trends.

Alfvénic intervals display a characteristic saturation in amplitude at the largest scales, suggesting a possible threshold for relative fluctuation growth. This saturation is consistently observed across all datasets. This saturation of amplitudes is expected in the presence of spherically polarized fluctuations with constant magnetic field magnitude (L. Matteini et al. 2015, 2018; C. Dunn et al. 2023). Indeed, Alfvénic wind is generally less magnetically compressible than non-Alfvénic wind, with relative $|\mathbf{B}|$ fluctuations remaining below 10%, although they tend to increase with radial distance. Non-Alfvénic intervals also exhibit an apparent amplitude saturation ($\delta B / \langle |\mathbf{B}| \rangle \approx 1$) but their distributions have long tails extending beyond $\delta B / \langle |\mathbf{B}| \rangle \gg 2$, contrary to Alfvénic wind (as also shown by L. Matteini et al. (2018)). Overall, non-Alfvénic wind is statistically more compressible than Alfvénic wind (up to three times the average rms values), with no clear radial dependence.

In contrast to magnetic field strength fluctuations, relative density fluctuations are enhanced closer to the Sun for Alfvénic wind, reaching relative amplitudes up to 30% at the largest scales ($30 \tau / \tau_c$) consistent with previous near-Sun observations (S. Zhao et al. 2021), and decreasing for the largest scales to less than 10% at 1 au. Non-Alfvénic intervals instead exhibit similar levels of density fluctuations at the largest scales across radial distances.

II. Dependence of compressible fluctuations on radial distance and plasma beta

Although certain radial trends are observed in the above analysis, compressibility exhibit significant stream-to-stream variability. On the contrary, a stronger correlation with β is observed for compressibility-related fluctuations. Figure 3 presents the normalized rms of the magnetic field magnitude (top panels) and of the density fluctuations (middle

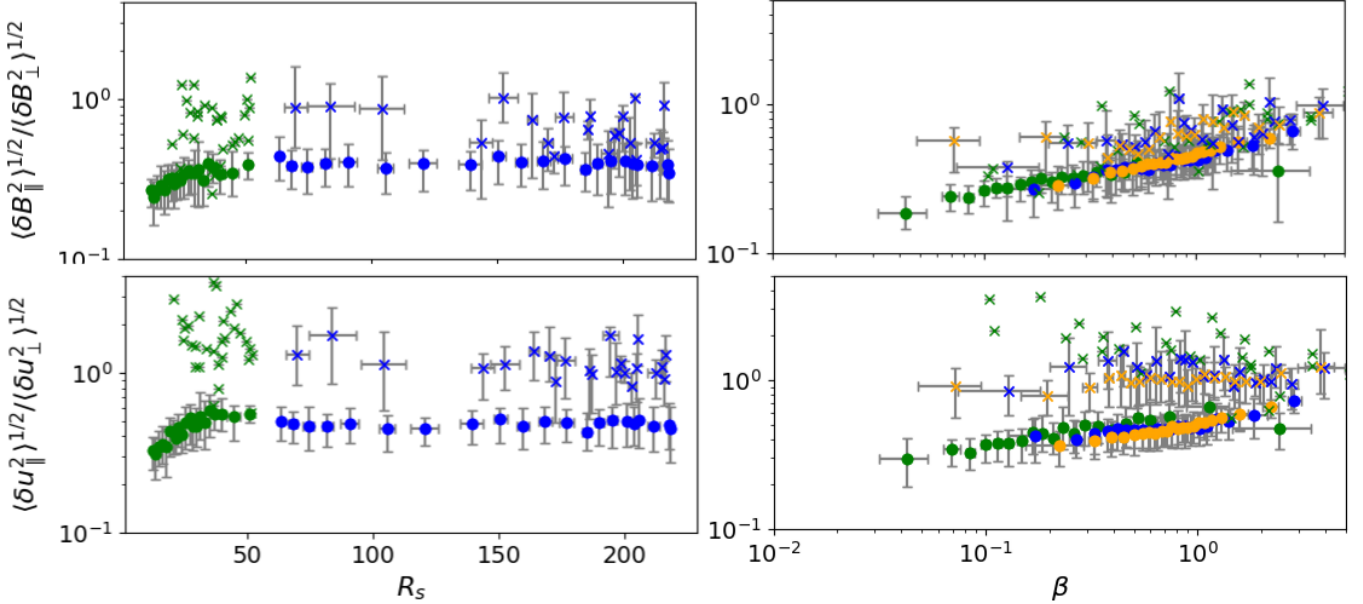


Figure 4. Ratios of the parallel to perpendicular component of magnetic field (top panels) and proton velocity (bottom panels) rms fluctuations as a function of radial distance (left) and plasma beta (right). Data points are obtained after averaging over each short sub-interval and binned, with bars indicating the variations of the data in each bin. Different colors are used to represent datasets from PSP (green), SolO (blue) and Wind (orange).

panels) computed for $\tau = 5\tau_c$. Each data point represents the ensemble average over a long sub-interval and shown as a function of the average proton β for each sub-interval. Similar results are found at individual time scales. We also plot the ratio $R_c = (\langle \delta n^2 \rangle^{1/2} / \langle n \rangle) / (\langle (\delta |\mathbf{B}|)^2 \rangle^{1/2} / \langle |\mathbf{B}| \rangle)$ (bottom panels). A strong correlation is obtained between magnetic compressibility and β across all datasets, with a Pearson correlation coefficient exceeding $\text{corr} > 0.5$. This dependence is consistent with previous findings (C. Chen et al. 2020; M. Brodiano et al. 2023). The density fluctuations also present a good correlation with β in the inner heliosphere, although the correlation weakens with increasing radial distance. This trend is evident for both Alfvénic and non-Alfvénic solar wind. Interestingly, the ratio R_c displays a stronger correlation with β than either measure alone, with $\text{corr} > 0.8$ in both Alfvénic and non-Alfvénic intervals.

We investigated the relative importance of the field aligned component in the magnetic and velocity field fluctuations, often associated to compressible fluctuations, relative to the transverse component, which contains mostly the Alfvénic contribution. Figure 4 shows the ratio between the rms of the parallel and perpendicular components as a function of R (left column) and β (right column) calculated at the same scale $\tau = 5\tau_c$ but by using the short sub-intervals to improve statistics. Instead of showing individual data point, the data were grouped into bins, and we show the mean value of each

bin. The gray bars represent the spread of data within each bin, calculated using the 16th and 84th percentiles.

For the Alfvénic wind, we observe that although the ratio remains significantly below unity, field-aligned fluctuations increase near the Sun compared to the transverse fluctuations up to $R \approx 50R_s$, and then their ratio saturates at a nearly constant value around 0.48 at larger distances. This behavior is consistent with the observed radial scalings laws of fluctuations already discussed in Section I. On the contrary, the ratio of field-aligned to transverse fluctuations in the non-Alfvénic wind does not show a well defined trend with radial distance and is characterized by large values of δB_{\parallel} and δv_{\parallel} , which are comparable to, or even larger than, the perpendicular component.

Interestingly, the previous observed dependence with β for compressible fluctuations (Fig. 3) is also found here for the Alfvénic wind in both magnetic and velocity field data, and in the magnetic field data for the non Alfvénic wind. The plots on the right column show a clear monotonic dependence of the fluctuations ratios with β that is distinct from the radial trends, and that qualitatively follows the trend of slow magnetosonic modes.

This result further suggests that the evolution of field-aligned fluctuations in the magnetic field might be the result of the contribution from both expansion effects on spherically polarized states and local mechanisms controlled by the plasma beta.

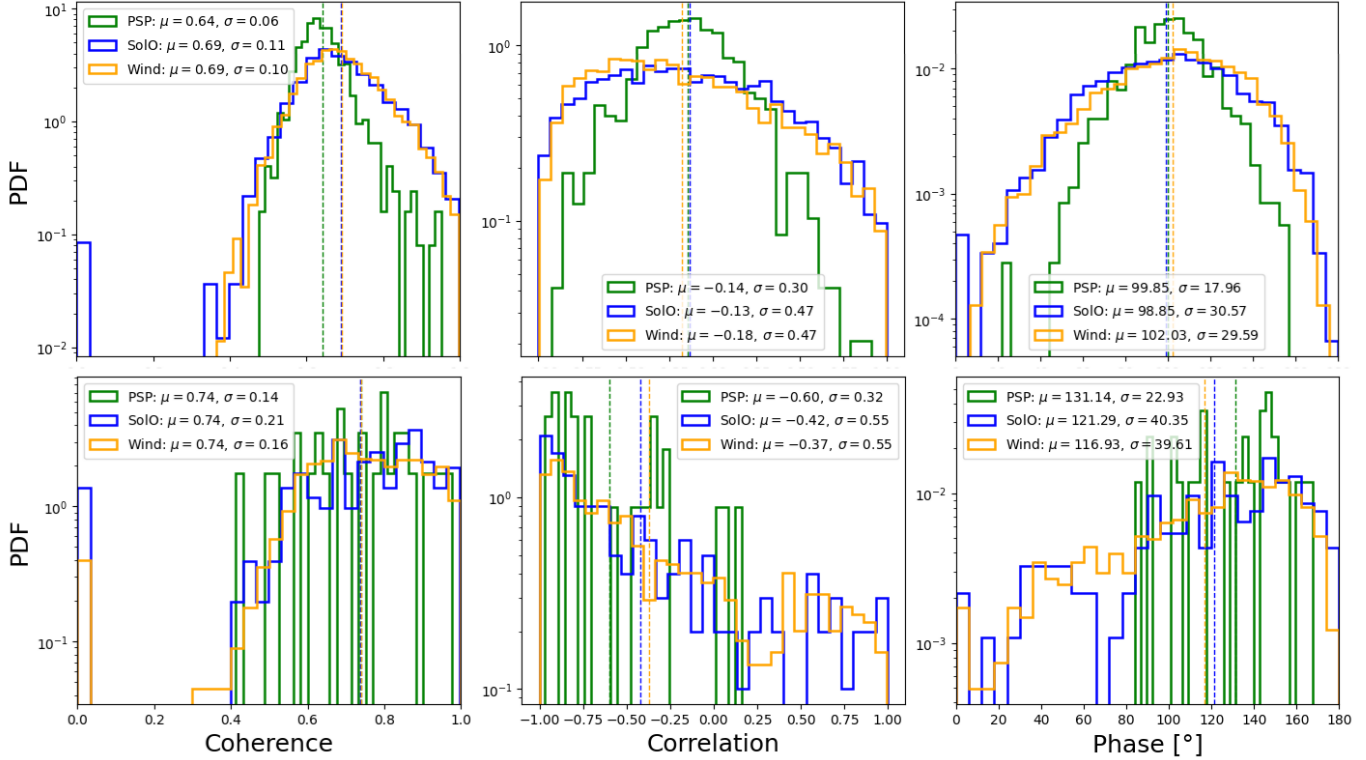


Figure 5. Distribution of correlation measures of compressible fluctuations for Alfvénic (top) and non-Alfvénic intervals (bottom). The panels show the PDFs of coherence (left), Pearson correlation (middle), and phase angle between $\delta n/\langle n \rangle$ and $\delta(|\mathbf{B}|^2)/\langle |\mathbf{B}|^2 \rangle$ (right). Results are shown for Wind (orange), Solo (blue), and for PSP (green). The legends show the mean and the standard deviation for each distribution.

III. Statistical analysis of compressible fluctuations

To characterize compressible fluctuations, we computed the coherence and phase between $\delta(|\mathbf{B}|^2)/\langle |\mathbf{B}|^2 \rangle$ and $\delta n/\langle n \rangle$ using the wavelet analysis for each short sub-interval (see Sec. 2). In addition, we also quantified the linear correlation between magnetic and plasma compressible fluctuations by calculating the Pearson correlation. For this analysis, we considered fluctuations at the scale $\tau = 5\tau_c$, and the average coherence and phase between them are computed across the frequency range $1/5 < \omega \tau_c < 1$ and over each entire sub-interval. This methodology allows us to identify the coherence and phase at the scale of interest and determine whether the fluctuations are in or out of phase, providing insight into the polarization of compressible modes. For reference, Fig. A2 shows an example of a wavelet analysis performed on an Alfvénic short sub-interval from the Wind database.

Figure 5 shows the distribution of the correlation measures for both Alfvénic and non-Alfvénic intervals. Table 2 summarizes additional statistical information including the fraction of sub-intervals with strong positive or negative correlation ($|\text{corr}| > 0.5$) and those with weak correlation ($|\text{corr}| < 0.5$), filtered by $C > 0.5$.

The table also lists the mean values of the phase $\langle \phi^\pm \rangle$ and $\langle \theta_{kB_0}^\pm \rangle$ for each group. By eye inspection of some selected sub-intervals, we found that low-correlation ($|\text{corr}| < 0.5$) is often due to the simultaneous presence of both positive and negative correlated fluctuations within the 2-hour sub-interval considered that, when averaged over the length of the sub-interval, reduce the correlation. For this reason we believe that data with $|\text{corr} < 0.5|$ still contain important information. Keeping these data is particularly relevant for the Alfvénic wind that shows a larger fraction of weakly correlated sub-intervals than the non-Alfvénic wind.

This statistical analysis shows that, at the scales considered, the compressible fluctuations are generally highly coherent across all datasets in both turbulent regimes. Within the non-Alfvénic intervals, we find similar statistical behavior at different heliocentric distances. Most of these intervals exhibit strong anti-correlation (with phase angles greater than 140°), characteristic of slow-mode fluctuations. A smaller fraction of intervals displays positive correlation and is nearly in phase, consistent with fast mode-like fluctuations.

By examining only intervals with strong correlations ($|\text{corr}| > 0.5$), it is evident that most of the non-Alfvénic solar wind is primarily composed of negatively corre-

mission	Alfvénic					
	portion ⁺	portion ⁻	$\langle \phi^+ \rangle$	$\langle \phi^- \rangle$	$\langle \theta_{kB0}^+ \rangle$	$\langle \theta_{kB0}^- \rangle$
corr > 0.5						
Wind	10.49%	29.68%	50.08°	133.22°	48.70°	54.55°
SolO	11.30%	25.61%	50.31°	134.74°	49.46°	51.68°
PSP	2.17%	10.84%	60.07°	129.12°	29.54°	31.78°
corr < 0.5						
Wind	22.05%	35.63%	79.38°	105.75°	51.68°	53.84°
SolO	26.22%	33.91%	77.86°	105.53°	48.70°	50.21°
PSP	27.30%	59.06%	82.46°	104.09°	32.86°	31.78°
Non-Alfvénic						
corr > 0.5						
Wind	11.82%	53.47%	45.46°	145.10°	58.67°	55.94°
SolO	10.39%	55.19%	47.56°	146.93°	66.42°	64.53°
PSP	0.0	60.00%		147.82°		43.11°
corr < 0.5						
Wind	9.90%	20.97%	82.53°	109.35°	60.66°	56.63°
SolO	6.49%	19.48%	85.16°	111.72°	61.96°	54.55°
PSP	6.67%	26.67%	84.93°	110.91°	52.41°	27.12°

Table 2. Summary of statistical results grouped by correlation sign in the Alfvénic and non-Alfvénic wind datasets. The table reports, for each type of wind, the fraction of intervals with positive and negative correlation, together with the ensemble-averaged phase and angle between the mean magnetic field and the solar wind velocity. Results are presented for both highly correlated and weakly correlated periods within each wind type.

lated intervals. In fact, at the scales considered here, no positively correlated intervals were identified in the PSP data, and only a minor contribution is seen farther out. This supports the conclusion that slow modes are the dominant compressible component in non-Alfvénic, balanced turbulent solar wind.

The Alfvénic solar wind exhibits characteristics similar to the non-Alfvénic intervals, with a larger fraction of data characterized by anti-correlated fluctuations than by positively correlated ones. Nonetheless, in most Alfvénic intervals fluctuations are either uncorrelated or only weakly correlated. Across all datasets (PSP, SolO and Wind with weak correlation), these intervals maintain an approximately mean phase of $\phi^+ \approx 78.99^\circ$ for positively and $\phi^- \approx 104.94^\circ$ negatively correlated cases.

When aggregating both strong and weak correlations, we find that the Alfvénic wind exhibits $\approx 30\%$ fast-type fluctuations, compared to $\approx 20\%$ in the non-Alfvénic wind, and more than $\approx 60\%$ of the fluctuations are of the slow-type in both winds, reaching $> 70\%$ in the slow wind. This may indicate that imbalanced turbulence systematically favors the generation of fast-type modes compared with balanced turbulence, although the slow mode is dominant in both winds.

To explore the source of compressibility, we analyzed the response of density fluctuations to variations in magnetic pressure. This was quantified by creating a scat-

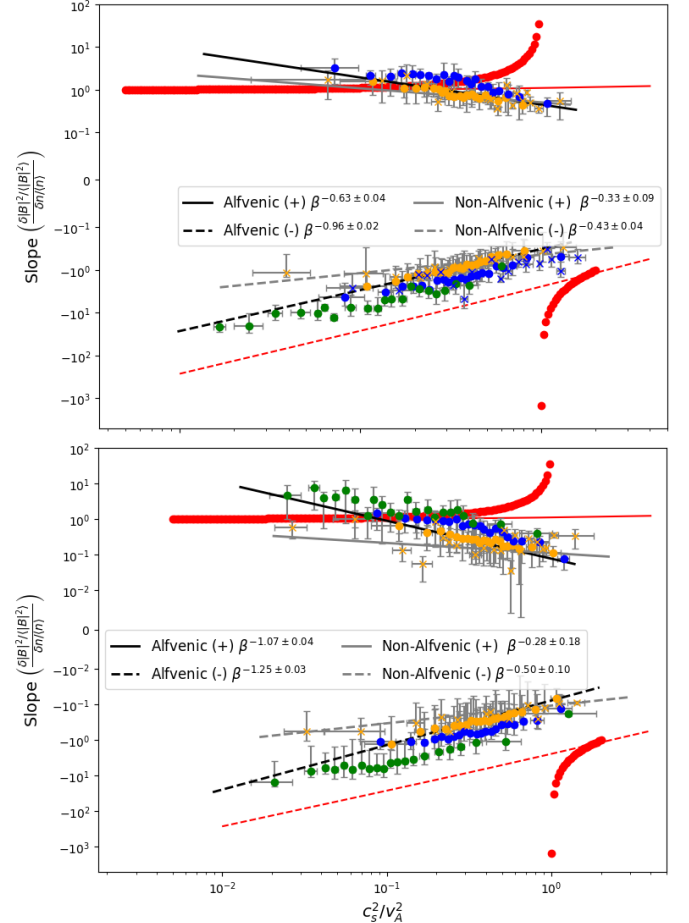


Figure 6. The response of density fluctuations to magnetic pressure variations in Alfvénic wind (circles) and non-Alfvénic wind (crosses). The top panel correspond to intervals with high correlation ($\text{corr} > 0.5$), while the bottom panel show those with low correlation ($\text{corr} < 0.5$). The error bars shows the standard deviations in the slope and c_s^2/v_A^2 values represented by each bin. The best fit of the combined data with positive and negative slopes is shown using the black and gray lines, respectively. We also plot the expected response from fast (red solid) and slow (red dashed) linear MHD modes for waves propagating at 60° . The response prediction from forced modes are shown using red dots.

ter plot of $\delta n/\langle n \rangle$ against $\delta(|\mathbf{B}|^2)/\langle |\mathbf{B}|^2 \rangle$ for each short sub-interval, from which we derived the value of the slope from their best linear fit (see bottom-left panel in Fig A2). Sub-interval were then categorized based on whether they exhibited a positive or negative slope. Figure 6 displays the results for both Alfvénic and non-Alfvénic intervals with $|\text{corr}| > 0.5$ (top panel) and $|\text{corr}| < 0.5$ (bottom panel). We grouped the data into 20 bins, representing values from all sub-intervals with similar slopes and beta values.

This analysis reveals a strong dependence on β , with low- β streams exhibiting a stronger response. This trend appears in both positively and negatively correlated periods and remains robust under both Alfvénic and non-Alfvénic solar wind conditions. While magnetic compressibility is generally small in the near-Sun, the low- β values there allow for an enhanced response, which may explain the larger density fluctuations seen in PSP data than further out. We calculated the best fits for fast and slow mode-like fluctuations, as indicated in the figure legends and plotted the regression line in black and gray colors for Alfvénic and non-Alfvénic wind, respectively. For reference, we also display with red solid and dashed curves the linear MHD prediction for the relation between density and magnetic fluctuations for the fast (+) and slow (−) modes,

$$\delta n/\langle n \rangle = v_A^2/(v_{ph}^2 - c_s^2) \delta B_{\parallel}/|\langle \mathbf{B} \rangle|, \quad (1)$$

where the square phase speed is

$$v_{ph}^2 = \frac{1}{2} \left[(v_A^2 + c_s^2) \pm \sqrt{(v_A^2 + c_s^2)^2 - 4v_A^2 c_s^2 \cos^2(\theta_{kB_0})} \right],$$

with v_A and c_s the Alfvén and sound speed and $c_s^2/v_A^2 = \gamma\beta_T/2$ (where we fix $\gamma = 1$ and β_T is the total plasma beta that we approximate as $\beta_T \approx 2\beta$) (A. A. Schekochihin 2022b; K. Lee & L. Lee 2020). We used the mean $\theta_{kB_0} = 60^\circ$ as reference value for the propagation angle. We further show as red dots the expected trend of density fluctuations driven nonlinearly by an amplitude-modulated Alfvén wave predicted by MHD theory (R. H. Cohen & R. M. Kulsrud 1974; J. V. Hollweg 1971; S. R. Spangler & J. P. Sheerin 1982)

$$\delta n/\langle n \rangle = (1 - c_s^2/v_A^2)^{-1} \delta(|\mathbf{B}|^2)/|\langle \mathbf{B} \rangle|^2. \quad (2)$$

We observe that intervals with negative correlation exhibit an approximate β^{-1} scaling (shown as a red dashed line), in line with the predictions of MHD slow-mode theory (D. Verscharen et al. 2017). Although the non-Alfvénic wind exhibit shallower slopes, the PSP and SolO measurements still robustly follow an overall $1/\beta$ trend even in this case. This result implies that compressible fluctuations, both close to the Sun and at larger heliocentric distances, retain characteristics consistent with MHD-like slow modes. Since these intervals represent the majority of the dataset, we can argue that the slow mode is the most significant contributor to compressible fluctuations in the solar wind.

In contrast, the positively correlated intervals do not display the MHD behavior anticipated from linear (shown as solid red line) or nonlinear (red dots) theory. The non-Alfvénic wind approaches the prediction

of fast magnetosonic mode, with a shallower slope than β^{-1} , but still steeper than predictions. Instead, we find that in the Alfvénic wind fluctuations follow a nearly β^{-1} scaling, both for the full data set and for each mission considered separately. This feature is especially important for intervals with $|\text{corr}| < 0.5$, which constitute the majority of the positively correlated sample in the Alfvénic wind, as indicated in Table 2. Furthermore, we do not observe the predicted transition from positive to negative correlation at a specific critical β , as would be expected if the compressive response was driven by amplitude-modulated Alfvén waves. Thus, contrary to the slow-type fluctuations, at least at the level of our fits, the observations of fast-type correlated fluctuations do not match current theoretical expectations for fast MHD modes and we do not find trends that are consistent with MHD theory of forced compressible modes. Additional theoretical and numerical work, exploring different dimensionalities and geometries (including the effects of expansion), as well as extensions to kinetic theory is likely required to better understand the nature of the fast modes observed in the data.

4. SUMMARY AND CONCLUSIONS

In this work we studied the statistical properties of compressible fluctuations in the solar wind using *in-situ* measurements obtained from PSP, SolO, and Wind missions, covering radial distances ranging from 10 solar radii to 1 au. We identified streams dominated by balanced and imbalanced turbulence in which the Alfvénic properties ($|\sigma_c| < 0.25$ and $|\sigma_c| > 0.75$) remained approximately constant for at least 30 correlation times. This methodology enabled us to analyze large-scale properties while reducing the mixing of streams from different origins and plasma conditions. We analyzed the radial scaling of magnetic field, magnetic field magnitude and density fluctuations, and compared with theoretical predictions of MHD waves. We also studied the scale dependence of the fluctuations amplitude and the level of compressibility at different radial distances and as a function of plasma beta. Finally, we performed a statistical analysis of the properties of compressible fluctuations in the solar wind.

We found that magnetic compressibility is low near the sun and increases with heliocentric distance, whereas density fluctuations show the opposite trend, exhibiting enhanced plasma compressibility closer to the sun. By analyzing how these quantities correlate with radial distance and β , we argued that this behavior likely results from a combination of expansion effects and compressible dynamics governed by local plasma conditions. As the solar wind expands, relative density fluctuations are

expected to decrease with distance or be reduced by kinetic damping. In contrast, small but finite magnetic field magnitude fluctuations are influenced by the radial increase of $\delta B/|\langle \mathbf{B} \rangle|$. Together, these two effects may explain the opposite radial trends of plasma and magnetic compressibility. However, the strong correlation of density and magnetic pressure fluctuations (Fig. 3), as well as of the ratio $\delta B_{\parallel}/\delta B_{\perp}$ (Fig. 4), with plasma β indicates that, in addition to the global radial evolution, local compressible processes controlled by β also play an important role.

A statistical analysis of the correlation, coherence and phase between density and magnetic pressure fluctuations shows that both solar wind types exhibit highly coherent compressible fluctuations displaying positive or negative correlation (Fig. 5 and Table 2). Non-Alfvénic intervals are dominated by anti-correlated fluctuations, which account for more than 70% of the short sub-intervals. In contrast, Alfvénic intervals contain a mixture of positively and negatively correlated compressible fluctuations, although the negatively correlated ones remain prevalent. Comparison between with MHD predictions for the relation between density and magnetic pressure fluctuations as a function of β (Fig. 6) indicates that the dominant anti-correlated fluctuations are consistent with slow MHD magnetosonic modes, whereas the positively correlated fluctuations are not reproduced by either linear or nonlinear MHD models. Because slow modes also dominate in the Alfvénic wind, the observed trend of $\delta B_{\parallel}/\delta B_{\perp}$ versus β (Fig. 4, top right panel) is likewise consistent with slow-mode magnetosonic behavior. Since β is generally lower at PSP than at larger heliocentric distances, this dominance can also account for the enhanced density fluctuations observed in the Alfvénic wind by PSP, together with the radial increase in $\delta B_{\parallel}/\delta B_{\perp}$ and the comparatively faster growth of magnetic pressure fluctuations inside $50, R_s$ (Fig. 4, top left panel; Table 1).

In conclusion, our analysis shows that density and magnetic pressure fluctuations are strongly influenced by plasma beta, demonstrating the presence of ongoing compressible dynamics within the expanding solar wind. Our results also support the idea that the enhanced density fluctuations observed near the Sun are produced by slow mode waves, which may contribute to solar wind heating and acceleration in that region P. J. Kellogg (2020); F. Mozer et al. (2022); P. Kellogg et al. (2024). A possible candidate for generating such fluctuations is parametric decay of Alfvén waves, which is expected to be favored in the low- β regions close to the sun (A. Tenerani et al. 2017; M. Shoda et al. 2019). In the Alfvénic wind, fast mode-like waves also contribute to the compressible component. These positively correlated fluctuations in density and magnetic pressure could arise from several mechanisms, particularly those associated with forced modes generated by Alfvén-wave steepening, which are especially relevant in Alfvénic wind. However, we do not observe theoretical features such as the predicted transitions between fast and slow modes at critical plasma beta (J. V. Hollweg 1971; R. H. Cohen & R. M. Kulsrud 1974; A. Mallet et al. 2021). These discrepancies motivate further comparisons with extended fluid and kinetic models, as well as numerical simulations.

ACKNOWLEDGMENTS

CAG acknowledges Daniel Ipia-Achury, Trevor Bowen, Alfred Mallet, Ben Altermann, and Nahuel Andres for their valuable discussions regarding the results presented in this work. This research was supported by NSF SHINE award number 2400967 and NSF CAREER award 2141564. We acknowledge Wind, Solar Orbiter and Parker Solar Probe missions for the use of the data publicly available at the [NASA Space Physics Data Facility](https://nasa-space-physics-data-facility). The CME catalog compiled by C. Möstl et al. (2020) is available at <https://helioforecast.space/icmecat>

REFERENCES

Asgari-Targhi, M., Asgari-Targhi, A., Hahn, M., & Savin, D. 2021, The Astrophysical Journal, 911, 63

Bale, S., Goetz, K., Harvey, P., et al. 2016, Space science reviews, 204, 49

Bavassano, B., & Bruno, R. 1989, Journal of Geophysical Research: Space Physics, 94, 11977

Bavassano, B., Dobrowolny, M., Mariani, F., & Ness, N. 1982, Journal of Geophysical Research: Space Physics, 87, 3617

Bavassano, B., Pietropaolo, E., & Bruno, R. 2000, Journal of Geophysical Research: Space Physics, 105, 15959

Bavassano, B., Pietropaolo, E., & Bruno, R. 2004, Annales Geophysicae, 22, 689, doi: [10.5194/angeo-22-689-2004](https://doi.org/10.5194/angeo-22-689-2004)

Belcher, J., & Davis Jr, L. 1971, *Journal of Geophysical Research*, 76, 3534

Brodiano, M., Dmitruk, P., & Andrés, N. 2023, *Physics of Plasmas*, 30

Bruno, R., & Carbone, V. 2013, *Living Reviews in Solar Physics*, 10, 1

Buti, B., Velli, M., Liewer, P., Goldstein, B. E., & Hada, T. 2000, *Physics of Plasmas*, 7, 3998

Chandran, B. D. 2008, *The Astrophysical Journal*, 685, 646

Chaston, C., Bonnell, J., Bale, S., et al. 2020, *The Astrophysical Journal Supplement Series*, 246, 71

Chen, C., Bale, S., Bonnell, J., et al. 2020, *The Astrophysical Journal Supplement Series*, 246, 53

Chiba, S., Shoda, M., & Imamura, T. 2025, *Astronomy & Astrophysics*, 695, A192

Cohen, R. H., & Kulsrud, R. M. 1974, *The Physics of Fluids*, 17, 2215

Cranmer, S. R., & Molnar, M. E. 2023, *The Astrophysical Journal*, 955, 68

Derby Jr, N. F. 1978, *Astrophysical Journal*, Part 1, vol. 224, Sept. 15, 1978, p. 1013-1016., 224, 1013

Dunn, C., Bowen, T. A., Mallet, A., Badman, S. T., & Bale, S. D. 2023, *The Astrophysical Journal*, 958, 88

D'amicis, R., Matteini, L., & Bruno, R. 2019, *Monthly Notices of the Royal Astronomical Society*, 483, 4665

D'Amicis, R., Matteini, L., Bruno, R., & Velli, M. 2020, *Solar Physics*, 295, 46

Gary, S. P. 1993, *Theory of space plasma microinstabilities* No. 7 (Cambridge university press)

Goldstein, M. L. 1978, *Astrophysical Journal*, Part 1, vol. 219, Jan. 15, 1978, p. 700-704., 219, 700

González, C.A. Tenerani, A., Matteini, L., Hellinger, P., & M., V. 2021, *The Astrophysical Journal Letters*, 914, L36

González, C., Innocenti, M. E., & Tenerani, A. 2023, *Journal of Plasma Physics*, 89, 905890208

González, C., Verniero, J., Bandyopadhyay, R., & Tenerani, A. 2024, *The Astrophysical Journal*, 963, 148

Hada, T. 1993, *Geophysical research letters*, 20, 2415

Hahn, M., D'Huys, E., & Savin, D. W. 2018, *The Astrophysical Journal*, 860, 34

Hollweg, J. V. 1971, *Journal of Geophysical Research*, 76, 5155

Hollweg, J. V. 1994, *Journal of Geophysical Research: Space Physics*, 99, 23431

Horbury, T., O'brien, H., Blazquez, I. C., et al. 2020, *Astronomy & Astrophysics*, 642, A9

Howes, G., Bale, S., Klein, K., et al. 2012, *The Astrophysical Journal Letters*, 753, L19

Kellogg, P., Mozer, F., Moncuquet, M., et al. 2024, *The Astrophysical Journal*, 964, 68

Kellogg, P. J. 2020, *The Astrophysical Journal*, 891, 51

Klein, K., Howes, G., TenBarge, J., et al. 2012, *The Astrophysical Journal*, 755, 159

Lee, K., & Lee, L. 2020, *The Astrophysical Journal*, 904, 66

Lepping, R., Acuña, M., Burlaga, L., et al. 1995, *Space Science Reviews*, 71, 207

Lin, R., Anderson, K., Ashford, S., et al. 1995, *Space Science Reviews*, 71, 125

Livi, R., Larson, D. E., Kasper, J. C., et al. 2022, *The Astrophysical Journal*, 938, 138

Mallet, A., Squire, J., Chandran, B. D., Bowen, T., & Bale, S. D. 2021, *The Astrophysical Journal*, 918, 62

Maruca, B. A., Qudsi, R. A., Alterman, B., et al. 2023, *Astronomy & Astrophysics*, 675, A196

Matteini, L., Horbury, T., Pantellini, F., Velli, M., & Schwartz, S. 2015, *The Astrophysical Journal*, 802, 11

Matteini, L., Landi, S., Velli, M., & Hellinger, P. 2010, *Journal of Geophysical Research: Space Physics*, 115

Matteini, L., Stansby, D., Horbury, T., & Chen, C. H. 2018, *The Astrophysical Journal Letters*, 869, L32

Matteini, L., Tenerani, A., Landi, S., et al. 2024, *Physics of Plasmas*, 31

Matthaeus, W. H., & Goldstein, M. L. 1982, *Journal of Geophysical Research: Space Physics*, 87, 6011

Miyamoto, M., Imamura, T., Tokumaru, M., et al. 2014, *The Astrophysical Journal*, 797, 51

Moncuquet, M., Meyer-Vernet, N., Issautier, K., et al. 2020, *The Astrophysical Journal Supplement Series*, 246, 44

Möstl, C., Weiss, A. J., Bailey, R. L., et al. 2020, *The Astrophysical Journal*, 903, 92

Mozer, F., Bale, S., Cattell, C., et al. 2022, *The Astrophysical Journal Letters*, 927, L15

Narita, Y., & Marsch, E. 2015, *The Astrophysical Journal*, 805, 24

Owen, C., Bruno, R., Livi, S., et al. 2020, *Astronomy & Astrophysics*, 642, A16

Perrone, D., D'amicis, R., De Marco, R., et al. 2020, *Astronomy & Astrophysics*, 633, A166

Roberts, D., Goldstein, M., Klein, L., & Matthaeus, W. 1987, *Journal of Geophysical Research: Space Physics*, 92, 12023

Sagdeev, R. Z., & Galeev, A. A. 1969, *Nonlinear Plasma Theory*

Schekochihin, A. A. 2022a, *Journal of Plasma Physics*, 88, 155880501

Schekochihin, A. A. 2022b, *Lecture Notes for the Oxford MMathPhys/MScMTP programme*

Shoda, M., Suzuki, T. K., Asgari-Targhi, M., & Yokoyama, T. 2019, *The Astrophysical Journal Letters*, 880, L2

Spangler, S. R., & Sheerin, J. P. 1982, *Journal of plasma physics*, 27, 193

Tenerani, A., Sioulas, N., Matteini, L., et al. 2021, *The Astrophysical Journal Letters*, 919, L31

Tenerani, A., Velli, M., & Hellinger, P. 2017, *The Astrophysical Journal*, 851, 99

Torrence, C., & Compo, G. P. 1998, *Bulletin of the American Meteorological society*, 79, 61

Tu, C.-Y., & Marsch, E. 1994, *Journal of Geophysical Research: Space Physics*, 99, 21481

Tu, C.-Y., & Marsch, E. 1995, *Space Science Reviews*, 73, 1

Verdini, A., Grappin, R., & Montagud-Camps, V. 2019, *Solar Physics*, 294, 65

Verscharen, D., Chen, C. H., & Wicks, R. T. 2017, *The Astrophysical Journal*, 840, 106

Villante, U., & Vellante, M. 1982, *Solar Physics*, 81, 367

Yao, S., He, J.-S., Marsch, E., et al. 2011, *The Astrophysical Journal*, 728, 146

Zhao, L.-L., Silwal, A., Zhu, X., Li, H., & Zank, G. 2025, *The Astrophysical Journal Letters*, 979, L4

Zhao, S., Yan, H., Liu, T. Z., Liu, M., & Shi, M. 2021, *The Astrophysical Journal*, 923, 253

APPENDIX

A. ADDITIONAL FIGURES

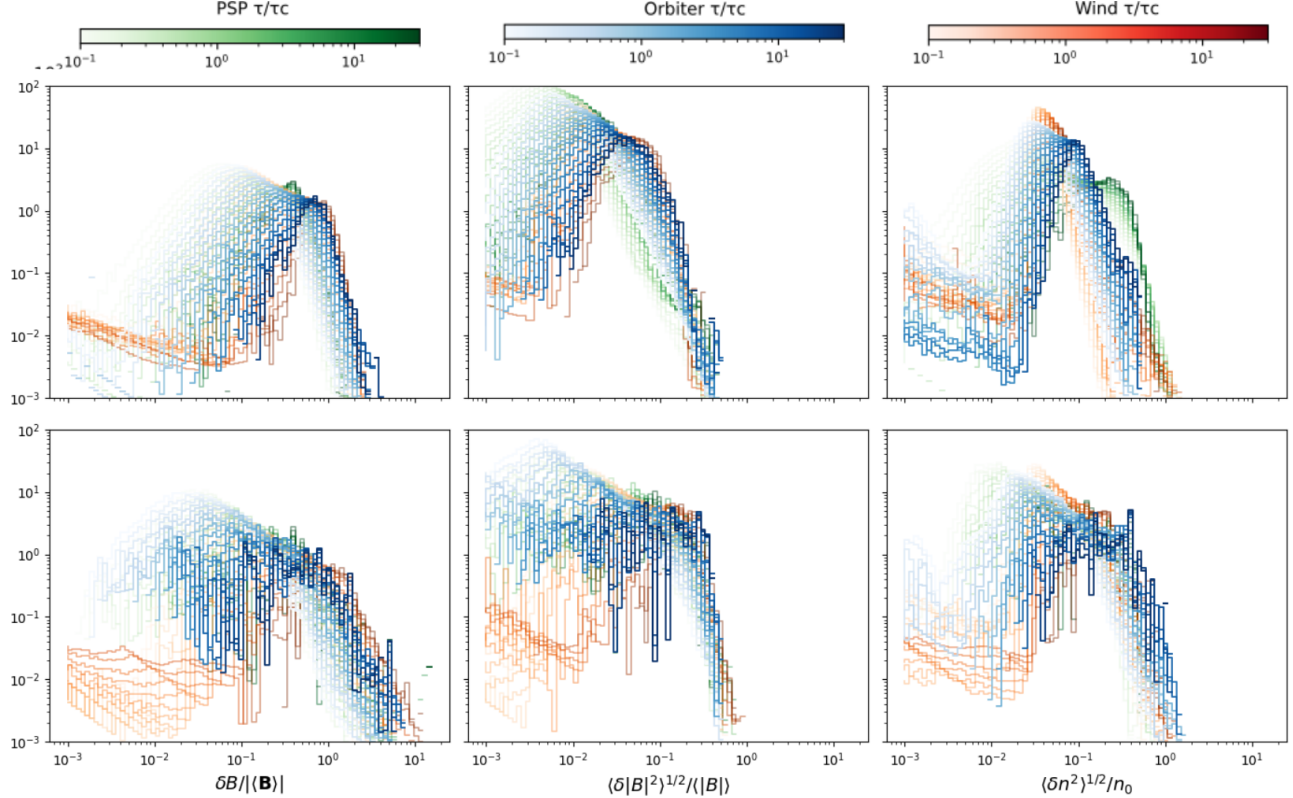


Figure A1. The PDF of the rms of the fluctuation's amplitude $\delta B/|\langle \mathbf{B} \rangle|$ (left), magnetic field magnitude fluctuations $\langle (\delta |\mathbf{B}|)^2 \rangle^{1/2}/|\langle \mathbf{B} \rangle|$ (middle), and of density fluctuations $\langle \delta n^2 \rangle^{1/2}/\langle n \rangle$ (right) for the Alfvénic (top panels) and non-Alfvénic (bottom panels). The color lines represent fluctuations over different time scales covering the range $0.1 < \tau/\tau_c < 30$.

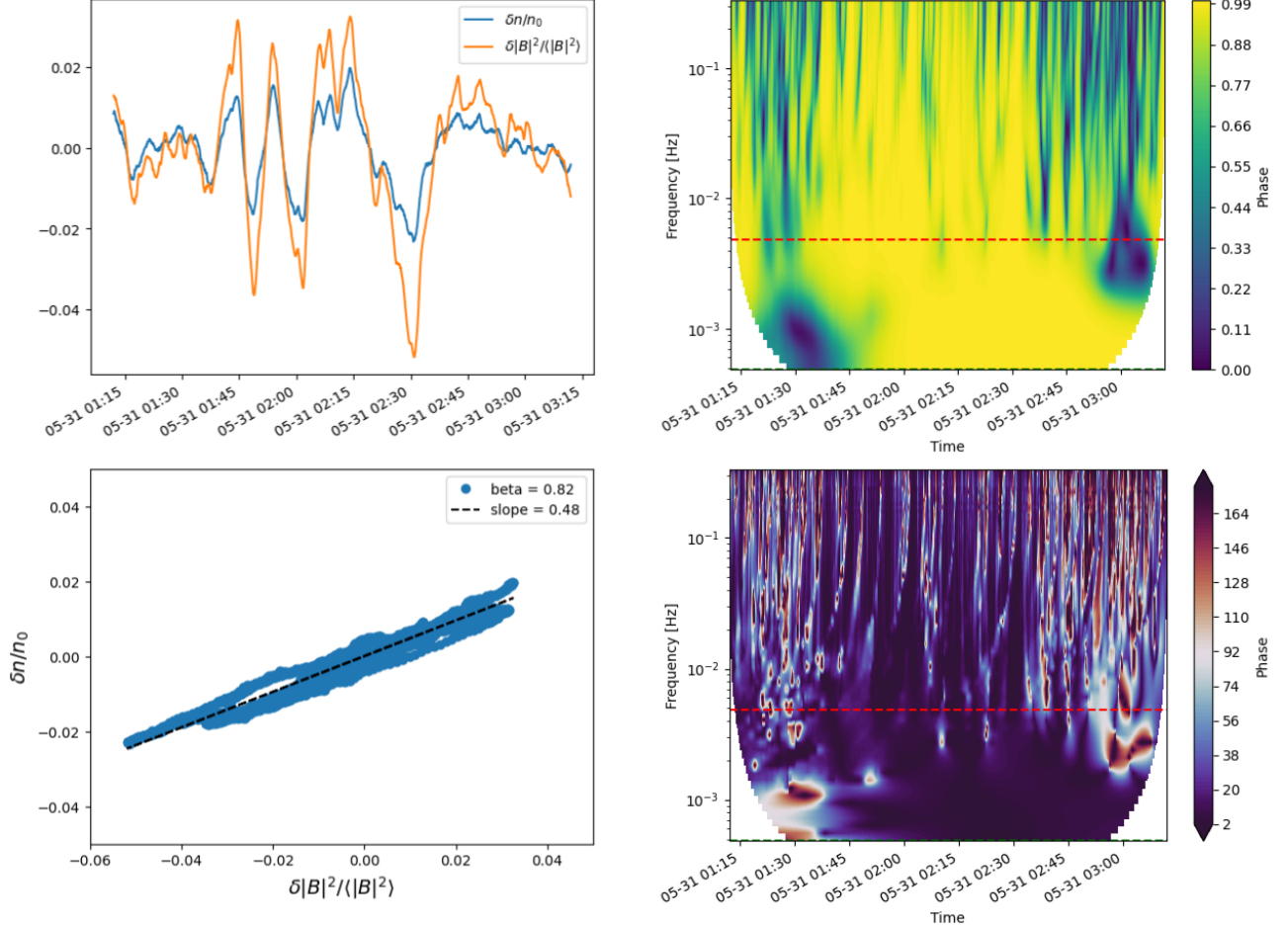


Figure A2. (Top Left) Time series of normalized density fluctuations ($\delta n/\langle n \rangle$) and magnetic pressure fluctuations ($\delta|B|^2/\langle|B|\rangle$) at the scale $\tau = 5\tau_c$ for an Alfvénic short sub-interval of Wind observations spanning 2000-05-31 01:12:03 to 2000-05-31 03:11:45. (Bottom Left) Scatter plot of $\delta n/\langle n \rangle$ versus $\delta|B|^2/\langle|B|\rangle$, with the legend indicating the mean proton beta and the linear fit slope between these two time series. The top-right panel show the spectrograms of the coherence ($C(t, \omega)$) and the bottom-right the phase ($\phi(t, \omega)$) between density and magnetic pressure fluctuations. The red dashed line mark the correlation time for that interval.